

Received August 7, 2020, accepted September 3, 2020, date of publication September 8, 2020,  
date of current version September 22, 2020.

Digital Object Identifier 10.1109/ACCESS.2020.3022624

# Airborne Multi-Channel Ground Penetrating Radar for Improvised Explosive Devices and Landmine Detection

MARÍA GARCÍA-FERNÁNDEZ<sup>✉</sup>, YURI ÁLVAREZ LÓPEZ<sup>✉</sup>, (Senior Member, IEEE),  
AND FERNANDO LAS-HERAS ANDRÉS<sup>✉</sup>, (Senior Member, IEEE)

Área de Teoría de la Señal y Comunicaciones, Departamento de Ingeniería Eléctrica, Universidad de Oviedo, 33203 Gijón, Spain

Corresponding author: Yuri Álvarez López (alvarezyuri@uniovi.es)

This work was supported in part by the Ministerio de Educación—Gobierno de España under Grant FPU15/06341, in part by the Ministerio de Defensa — Gobierno de España and the University of Oviedo under Grant 2019/SP03390102/00000204 / CN-19-002 (SAFEDRONE), in part by the Xunta de Galicia – Axencia Galega de Innovación (GAIN), (“RadioUAV: drones para aplicaciones más allá de lo visible”), under Grant 2018-IN855A 2018/10, in part by the Government of the Principality of Asturias (PCTI) and European Union (FEDER) under Grant IDI/2018/000191, and in part by the Instituto Universitario de Tecnología Industrial de Asturias (IUTA) under Grant SV-19-GIJON-1-17 (RadioUAV).

**ABSTRACT** An improved Ground Penetrating Radar (GPR) system on board an Unmanned Aerial Vehicle (UAV) is presented in this contribution. The system has been designed for the detection and imaging of buried targets and, in particular, landmines and Improvised Explosive Devices (IEDs). Resting on the hardware and architecture of a previous aerial platform, in the proposed system the scanning area is increased and the detection capabilities are improved. These improvements are achieved by employing two receiving antennas and new processing techniques that increase the Signal-to-Clutter Ratio of the GPR images. Besides, parameters affecting the GPR image resolution, such as the flight speed and the amount of measurements that can be processed together using Synthetic Aperture Radar (SAR) techniques, are also studied. The developed system exhibits several advantages: safety and faster scanning speeds, together with the capability to detect both metallic and non-metallic targets, as shown in the examples presented in this contribution.

**INDEX TERMS** Ground penetrating radar (GPR), subsurface sensing and imaging, synthetic aperture radar (SAR), landmine detection, unmanned aerial vehicle (UAV), drones, real time kinematic (RTK).

## I. INTRODUCTION

Non-Destructive Testing (NDT) techniques have been of great interest in a wide scope of applications, from mining and geology, to civil engineering and civil works, archaeology, and security and defense, among others. NDT techniques allow to detect, locate, and, eventually, to obtain an image of the concealed object, avoiding the interaction with the object and the surrounding medium [1]. Among the different NDT systems, Ground Penetrating Radar (GPR) is one of the most powerful techniques for underground imaging thanks to its capability of providing images of the soil and the objects buried in it [1]. Similarly to other electromagnetic wave-based NDT techniques, GPR is based on detecting the impedance mismatch at the interface between two media.

The associate editor coordinating the review of this manuscript and approving it for publication was Francesco Benedetto<sup>✉</sup>.

This mismatch causes the reflection of the electromagnetic wave that hits the interface.

GPR systems can be classified according to the angle of illumination with respect to the soil/ground as follows:

i) Forward-looking GPR systems (FLGPR). The transmitting antenna illuminates the soil under a given angle of incidence, trying to minimize the reflection coming back from the air-soil interface [2], [3]. The angle between the radar antennas and the ground results in only a little part of the reflected energy being backscattered towards the radar. Therefore, FLGPR systems require high dynamic range at the receiver to achieve enough sensitivity to detect the buried targets.

ii) Down-looking GPR systems (DLGPR). The incident wave hits normally the ground interface [2], [4]. The distance from the radar to the ground is smaller than in FLGPR and they can provide better resolution. In general, the amount of

power backscattered by the buried targets is greater than in the case of FLGPR, but the clutter is also greater due to the reflection of the electromagnetic waves in the ground.

In the field of landmine and Improvised Explosive Devices (IEDs) detection, GPR systems have become an efficient solution as they are able to detect both metallic and non-metallic buried targets. In the last decades, different techniques have been proposed to improve the performance of GPR systems to detect landmines and IEDs [5]–[8]. Compared to other GPR applications, here the main challenge is to minimize the risk of detonation of landmines/IEDs, by keeping a safety distance with the area to be scanned (typically from 3 to 5 m in the case of terrestrial GPR scanners). Besides, the probability of detection has to be maximized. Thus, airborne-based GPR systems are a promising technology aiming to address the aforementioned challenges in landmine and IEDs detection.

#### A. UAV-BASED GPR SYSTEMS

Unmanned Aerial Vehicles (UAVs), commonly known as *drones*, have experienced a great development over the last years thanks to improvements in avionics and propulsion systems, capacity of batteries, autonomous navigation capabilities, and ease of sensor integration. Besides, the reduction on the cost of these devices have enabled the introduction of UAVs in several fields such as precision agriculture and forestry monitoring [9], [10], glaciology [11], ground observation and mapping [12]–[15] and electromagnetic compatibility and antenna measurements [16], [17]. In connection with the latter, UAVs can be used as well for network coverage and data connectivity improvement [18], [19].

These advances in UAV technology have made possible the development of UAV-based GPR systems for non-destructive testing and imaging of buried targets. This is of special interest in the field of landmine and IEDs detection. The main advantages of UAV-based GPR systems are: i) higher scanning speed compared to solutions based on terrestrial autonomous robots [20], [21]; ii) capability to scan difficult-to-access areas; and iii) safety, as contact with soil is avoided, thus minimizing the risk of accidental detonation.

First attempts to detect IEDs and landmines using airborne-based systems employed metal detectors [22]. However, metal detectors cannot detect explosives with low or no metal content, which limits the range of application of these systems. Thus, next step was the integration of a GPR on board a UAV [23].

The different scanning modes for UAV-based GPR systems are illustrated in Fig. 1 of [24], mainly FLGPR (or side-looking GPR) and DLGPR. The former has been widely used for landmine and IED detection, and it has been recently tested on board UAVs, as shown in [25] and in [24]. If a side-looking GPR system follows a circular path, Circular-based Synthetic Aperture Radar processing (CSAR) can be applied for imaging the ground and buried targets [26]. In the case of UAV-based DLGPR, [27], [28] propose to use a low-cost lightweight Stepped Frequency Continuous Wave radar

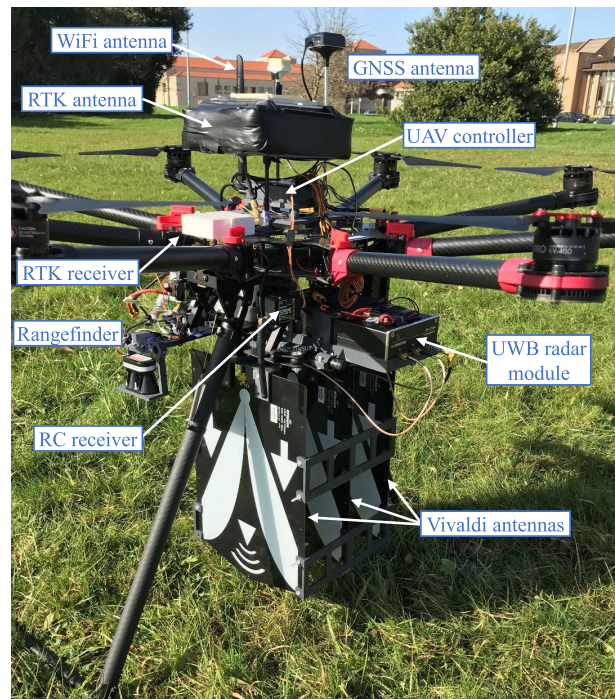


**FIGURE 1.** Picture of the implemented prototype, pointing out the main hardware components.

working in the 550 - 2700 MHz frequency band. Another prototype of interest, based on a Software Defined Radio (SDR)-GPR, is described in [29]. [30] makes use of a commercial GPR working at sub-GHz frequencies, thus providing more penetration depth but at the expense of losing spatial resolution.

Most UAV-based GPR systems consist of a compact GPR unit that stores geo-referred measurements for post-processing. Geo-referring accuracy affects the horizontal (cross-range) resolution of the GPR system. Besides, it should be within the order of half a wavelength to apply Synthetic Aperture Radar (SAR) processing, that is, to allow the coherent combination of the radar measurements taken at each position. The decrease in the cost of Global Navigation Satellite Systems (GNSS) - Real Time Kinematic (RTK) modules has led to their integration in the UAV hardware. RTK modules are able to provide centimeter-level positioning accuracy, thus enabling GPR-SAR processing. First results of UAV-based GPR-SAR are shown in [31], and they have been later extended to 3D GPR-SAR imaging in [32] and in [26] for the case of CSAR. Concerning the working frequency band, it ranges from 300 MHz to 5 GHz, as it provides a good trade-off between spatial resolution (a bandwidth of 4 GHz gives a range resolution of 75 mm) and penetration depth (taking into account that most IEDs and landmines are buried less than 50 cm deep).

In the field of UAV-based GPR systems, the extension from 2D to 3D scans is still limited by the flight autonomy of the UAVs, as in most of the aforementioned contributions the

**TABLE 1.** Comparison of UAV-based GPR systems.

Reference	Frequency band (GHz)	Architecture	Tested targets and soil	SAR processing	Imaging domain size
[26]	1 - 4	Side-looking GPR	Metallic and non-metallic. Sandy soil.	Yes. CSAR	3D (volume) Scanned area: 6.25 m × 5.25 m
[28]	0.55 - 2.7	DLGPR	Metallic and non-metallic. Loamy soil.	No SAR.	2D (vertical cut) One cut, length not indicated.
[29]	From ~1 to ~3	DLGPR	Metallic and non-metallic. Few cm deep. Loamy soil.	No SAR.	3D (volume) Low resolution. Scanned area: 7 m × 5 m
[30]	≤ 1 Narrow-band.	DLGPR	Metallic and non-metallic. Loamy soil.	No SAR.	3D (volume) Low resolution. Scanned area: Not indicated.
[31]	3 - 5	DLGPR	Metallic and non-metallic. Buried in a sandbox.	Yes.	2D (vertical cut) One cut, 2.5 m long.
[32]	0.6 - 6	DLGPR	Metallic. Loamy soil.	Yes.	3D (volume) Scanned area: 1 m × 4 m
This work	0.6 - 6	DLGPR 1 Tx 2 Rx	Metallic and non-metallic. Loamy soil.	Yes.	3D (volume) Scanned area: 1.6 m × 8 m

selected UAV provides an average flight-time of 15 minutes. In the few contributions presenting 3D GPR SAR results [26], [32], scanned areas per flight range from 5 m<sup>2</sup> to 40 m<sup>2</sup>. Thus, the scanning of larger areas would require other platforms such as wire-powered UAVs.

In order to provide a comparison of the current state-of-the-art in the field of UAV-based GPR systems, Table 1 summarizes the main features of the systems mentioned in this Section I-A.

### B. AIM AND SCOPE OF THIS CONTRIBUTION

Results presented in [32] and [26] prove the feasibility to detect buried targets using UAV-based GPR systems (DLGPR and side-looking GPR architectures, respectively), introducing SAR processing to achieve cm-level resolution. UAV-based GPR systems without SAR processing are limited in terms of cross-range resolution, being, in general, unable to detect targets whose size is smaller than 15-20 cm. The frequency bands of these systems provide a good trade-off between image resolution and penetration depth.

In this contribution, the system presented in [32] is improved aiming to achieve better detection capabilities and to increase the scanning area. First, a 3-element antenna array is mounted on board the UAV. One antenna is used for transmission and two for reception, as the radar module has two receiving channels. The employment of a dual-channel receiver entails a significant contribution in the field of UAV-based GPR systems as, up to the authors' knowledge, existing UAV-based GPR systems use a single transmitter and receiver. This allows performing the coherent combination of the SAR images associated to each of the two receiving channels of the radar module. Besides, radar processing is improved by applying a clutter filtering technique based on

Singular Value Decomposition (SVD) and a processing gain technique to increase the dynamic range. Finally, masked SAR processing is introduced to further mitigate the clutter when larger areas are scanned. All these combined improvements result in a Signal-to-Clutter Ratio improvement, which allows a better detection of buried targets.

## II. UAV-BASED UNDERGROUND SAR IMAGING SYSTEM IMPLEMENTATION

### A. OVERVIEW OF THE AIRBORNE-BASED GPR SYSTEM

The UAV-based GPR prototype is based on the architecture described in [32]. The main systems and subsystems of the prototype are:

- Flight control subsystem. It consists of a micro-computer (Raspberry Pi), with an add-on board [33] to act as UAV flight controller. This add-on board includes positioning sensors usually mounted on UAVs: an Inertial Measurement Unit (IMU), a barometer and a GNSS receiver.
- Accurate positioning subsystem to provide cm-level accuracy. It comprises a LIDAR (Light Detection And Ranging) altimeter (or rangefinder) and a dual-band RTK-GNSS system [34]. The latter is composed by an RTK antenna and an RTK receiver. RTK corrections are received from a GNSS base station and sent to the RTK receiver. A dual-band RTK was chosen as it provides better accuracy and availability (that is, percentage of time that corrected coordinates are provided), more robustness (e.g. when working in limited sky view areas), and faster deployment time compared to single-band RTKs. Concerning RTK accuracy, it is around 0.5 cm in the horizontal plane and 1 cm in the vertical direction [32]. With respect to LIDAR, estimated accuracy is around 1.8 cm [31].
- Radar subsystem. A lightweight, compact Ultra Wide Band (UWB) radar, whose frequency band ranges from 100 MHz to 6 GHz [35], was selected. This radar has one transmitting port, and two receiving ports. Thus, taking advantage of the number of ports, the radar is connected to a 3-element antenna array. Each antenna is a UWB Vivaldi antenna working in the 600 MHz to 6 GHz frequency band [36].
- A ground station, consisting of a conventional laptop, which receives the radar measurements and positioning and geo-referring information. Geo-referred measurements are processed using a GPR-SAR imaging algorithm to create radar images of the underground and objects buried in it. The processing algorithm is described in Section II-B.
- Communication subsystem, composed by a data link and a radio-control link. The data link, that is, the communication between the UAV and the laptop acting as ground station, is based on an in-situ deployed Wireless Local Area Network (WLAN). This WLAN can be set to work at 2.4 GHz or 5.8 GHz. Thanks to the DLGPR

configuration and the use of directive antennas, interferences between the radar and the WLAN are negligible, apart from the fact that both WLAN and UWB radar use spread spectrum signals. The in-situ deployed WLAN is connected to a mobile phone to enable Internet access, so RTK corrections from a GNSS base station can be received. Concerning the radio-control of the UAV, 433 MHz transmitting and receiving modules have been selected.

The UAV model allows mounting a payload up to 5 kg weight [37], providing capacity for further improvements of the prototype with additional sensors or devices (e.g. integration of more antennas, as in this contribution). The overall weight of the payload composed by the described systems and subsystems is about 3 kg (excluding batteries), resulting in about 15 minutes flight (similarly to the flight time achieved in [32]).

For the experimental validation shown in this contribution, only the frequency band from  $f_{min} = 600$  MHz to  $f_{max} = 3$  GHz was selected for radar data processing, since the soil losses in the measured scenario produce too much attenuation at higher frequencies.

Finally, a picture of the UAV taken after conducting a flight is shown in Fig. 1.

## B. DATA PROCESSING

The two main data sources of the UAV-based GPR system come from the positioning and geo-referring information subsystem and from the radar subsystem. The former are required to properly geo-refer radar measurements so that GPR-SAR processing can be applied. It is worth noting that the geo-referred radar measurements are sent in real-time to the ground-control station. A flowchart of the data processing is shown in Fig. 2.

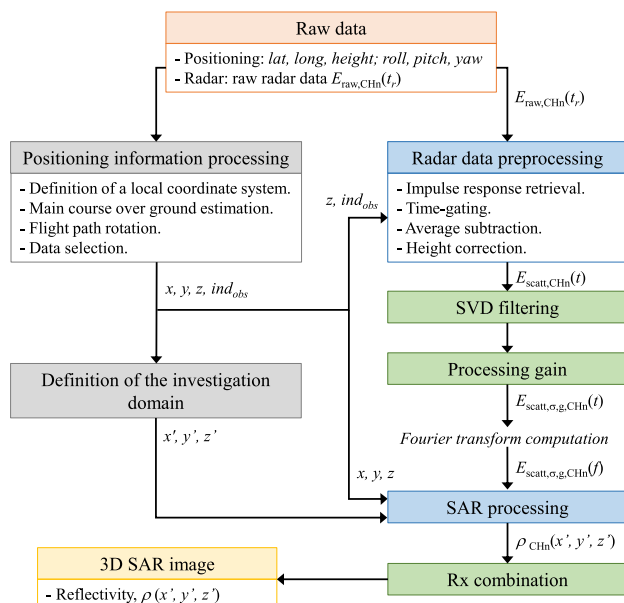


**FIGURE 2.** Data processing flowchart.

First, positioning information is processed, providing the  $x, y, z$  coordinates defined according to a local coordinate system (as explained in detail in [32]). Positioning information is also used to select the radar measurements that will be process ( $ind_{obs}$ ), mainly in order to avoid oversampling in some areas and to discard non-valuable data [38].

Concerning radar data processing, the basic preprocessing comprises: first, retrieving the impulse response; then, performing time-gating to select the range of interest; and, finally, applying average subtraction and height correction to mitigate the clutter.

In this contribution, the preprocessing stage is improved applying Singular Value Decomposition (SVD) filtering and processing gain techniques (as explained in Section III). After the preprocessing, the Fourier Transform is applied to transform the preprocessed radar data to the frequency domain.

Next, given the coordinates of the measurements ( $x, y, z$ ) and the investigation (or imaging) domain ( $x', y', z'$ ), SAR processing is applied to recover the reflectivity within the investigation domain for each channel  $n$  ( $n = 1, 2$ ) of the radar module ( $\rho_{CHn}(x', y', z')$ ).

Finally, both channels are coherently combined to obtain a single reflectivity set ( $\rho(x', y', z')$ ).

## III. IMPROVEMENTS IN DATA PROCESSING

### A. SVD FILTERING AND PROCESSING GAIN

In order to further mitigate the clutter whilst improving the dynamic range, SVD filtering and processing gain techniques are applied before the SAR processing.

Regarding SVD filtering, it consists of computing the SVD of the radar measurements for each channel and then discarding the data corresponding to the most significant singular values. The radar data matrix contains  $N_M$  radar measurements of  $N_S$  samples each. Then, applying SVD, the  $N_M \times N_S$  radar data matrix is decomposed into  $N_I = \min(N_M, N_S)$  eigenimages. Each eigenimage is associated to its corresponding singular value  $\sigma_i$ ,  $i = 1, \dots, N_I$  (where  $\sigma_1 > \sigma_2 > \dots > \sigma_{N_I}$ , i.e. the singular values are in descending order). The first eigenimages contain highly correlated information, which corresponds to the strong reflection from the air-soil interface and should be removed. The difficulty when applying SVD filtering is to choose how many eigenimages can be removed without losing information from the buried targets. In this contribution, a conservative procedure has been adopted and only the first eigenimage (associated to  $\sigma_1$ ) is removed. This helps to mitigate the clutter from the air-soil interface, while ensuring that the lost of information from the buried objects is minimized.

Then, a processing gain technique is applied to enhance the signal coming from the reflection at the buried objects (thus compensating the attenuation in the soil). The idea behind this technique is to introduce a gain function  $g(r)$  (where  $r$  denotes the range) so that the amplitude of the reflectivity is increased within a certain depth interval. In this contribution, a power gain function  $g(r)$  has been adopted. This function is

defined as follows:

$$g(r) = \begin{cases} r_0^\alpha, & r < r_0 \\ r^\alpha, & r_0 \leq r \leq r_1 \\ r_1^\alpha, & r > r_1 \end{cases} \quad (1)$$

where  $r_0$  is the initial depth at which the signal is amplified,  $r_1$  is the final depth, and  $\alpha$  is a coefficient that controls the value of the gain function. These parameters have been set to  $r_0 = -0.2$  m,  $r_1 = -1.2$  m and  $\alpha = 4$ . This means that the signal amplitude in the range  $[r_0, r_1] = [-0.2, -1.2]$  m is amplified by a factor of  $r^4$ .  $r_0$  is set to  $-0.2$  m to avoid amplifying air-soil reflections. As observed in GPR-SAR images (vertical cuts), the thickness of the air-soil reflection is around 10-12 cm (considering a  $-20$  dB reflectivity threshold). Regarding  $r_1$ , the threshold of  $-1.2$  m is chosen based on the maximum achievable penetration depth (actually in the scenario used in this contribution a lower  $r_1$  threshold could have been chosen due to the high moisture level of the soil). It is worth noting that the position  $r = 0$  m corresponds to the location of the air-soil interface.

An example of the impact of SVD filtering and processing gain is shown in Fig. 3. A set of 1000 radar measurements collected during a flight has been considered. Fig. 3 (a) shows the measurements after the radar data preprocessing and before applying SVD filtering and processing gain (see data processing flowchart of Fig. 2). Results after applying SVD filtering (where the first eigenimage, corresponding to the first singular value,  $\sigma_1$ , has been removed) are depicted in Fig. 3 (b). It can be noticed that the clutter due to the air-soil interface is reduced. Then, gain processing is applied, according to the function defined in (1). From the results shown in Fig. 3 (c), a reduction in the clutter level (and thus, an increase in the dynamic range) can be observed.

## B. SAR PROCESSING ENHANCEMENTS

SAR processing allows obtaining high-resolution radar images of the subsoil, thanks to the coherent combination of the measurements taken in the acquisition domain  $x, y, z$ . Range resolution ( $\Delta R_z$ ) is given by the radar subsystem bandwidth (BW) according to  $\Delta R_z = v_p/(2 \text{ BW})$  (where  $v_p$  is the propagation speed of the electromagnetic wave), whereas cross-range resolution ( $\Delta R_{x,y}$ ) depends on the vertical distance between the acquisition domain and the investigation domain ( $h$ ) and the size of the aperture to be considered within the acquisition domain ( $L_{x,y}$ ). Thus,  $\Delta R_{x,y} = \lambda h/L_{x,y}$ , where  $\lambda$  is the wavelength at the center frequency of the working frequency band.

One of the challenges faced with the improvements introduced in the new prototype is related to the larger size of the acquisition and investigation domains, if compared to previous works [31], [32]. For this reason, masked SAR processing has been introduced. It relies on computing the reflectivity on each voxel of the investigation domain considering only the acquisition domain points in the vicinity of the voxel, as depicted in Fig. 4. This approach helps to

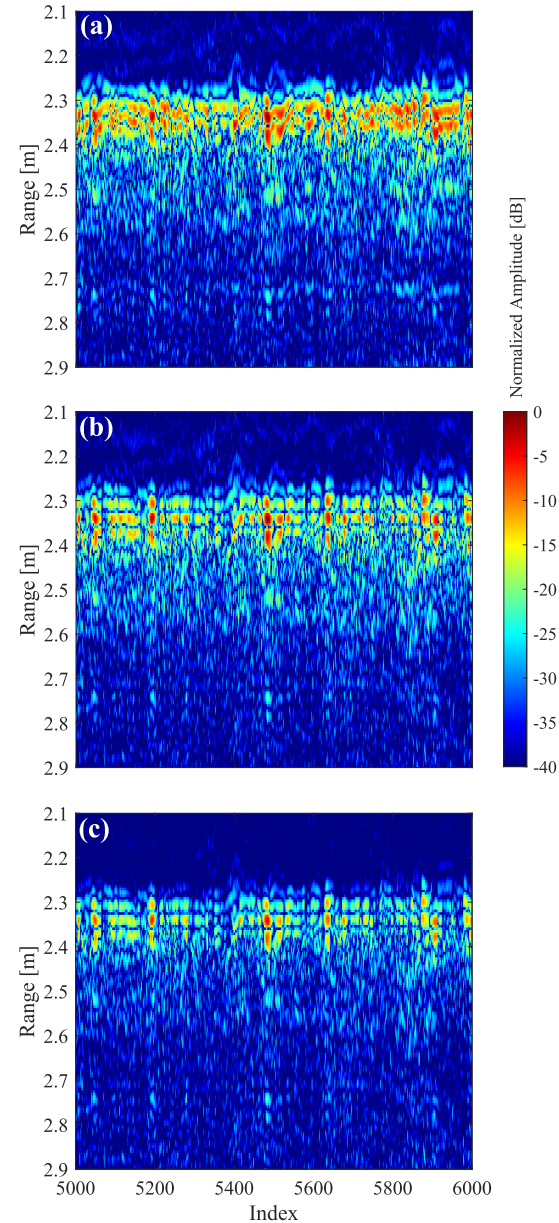


**FIGURE 3.** Example of radar measurements,  $E_{\text{scatt}}$  taken along a flight path (in these plots, the zero value of the vertical axis is set at the UAV position, i.e. 2.35 m above ground). Before SVD filtering and processing gain (a). After SVD filtering (b). After SVD filtering and processing gain (c).

mitigate the clutter, since the most relevant information for computing the reflectivity at a certain position is given by the measurements taken near to it. The size of the mask defining the measurements to be considered for each voxel depends on the coherence length along  $x$  and  $y$  axes, that is, the length along with radar measurements can be coherently combined.

As indicated in the data processing flowchart of Fig. 2, the output of the SAR processing stage is a set of two SAR images, one per each receiving channel of the radar. Clutter appearing in each SAR image can be further mitigate by coherently adding both SAR images, as the phase of the clutter on each individual channel is expected to be considerably uncorrelated. Besides, the phase corresponding to

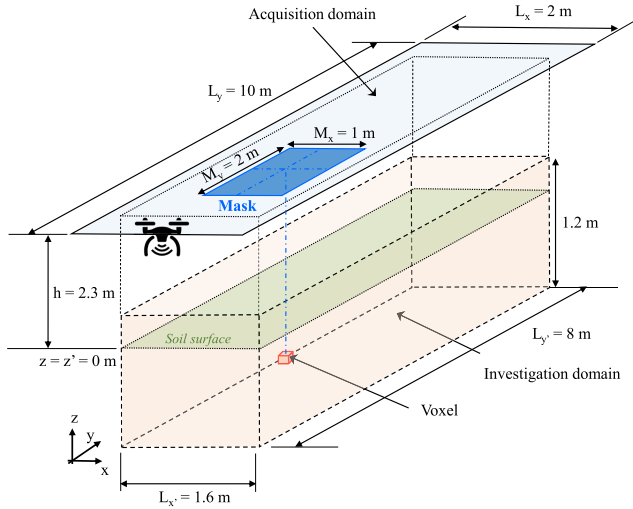


**FIGURE 4.** Scheme showing the acquisition domain (2D) and the investigation domain (3D), together with the concept of applying masks in the investigation domain for SAR processing. Dimensions correspond to the examples shown in Section IV.

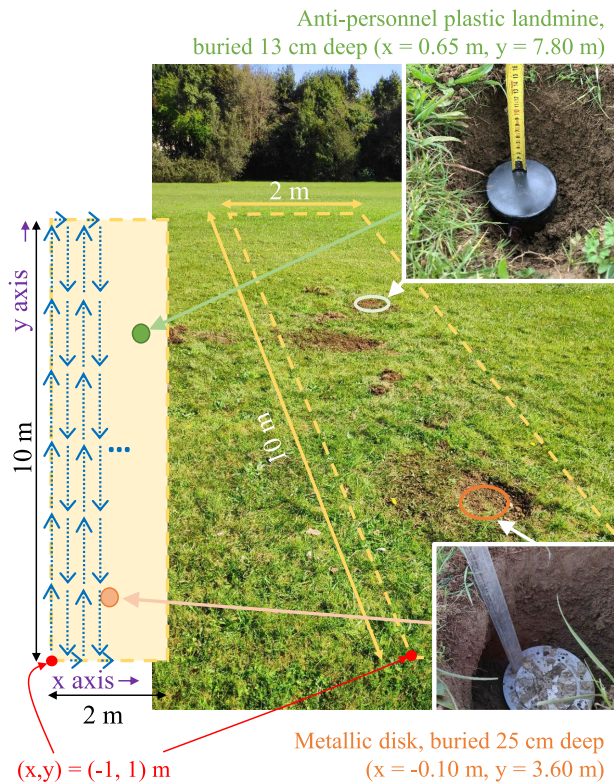


**FIGURE 5.** Picture of the scenario and buried targets: an anti-personnel plastic landmine, and a metallic disk. The scheme in the left side of the picture illustrates the flight path.

reflections on the targets will exhibit a high degree of correlation, so these reflections will be reinforced in the combined SAR image.

The antenna array placed on board the UAV (see Fig. 1) consists of three UWB Vivaldi antennas spaced 9.8 cm. The outer antennas are connected to the receiving channels of the

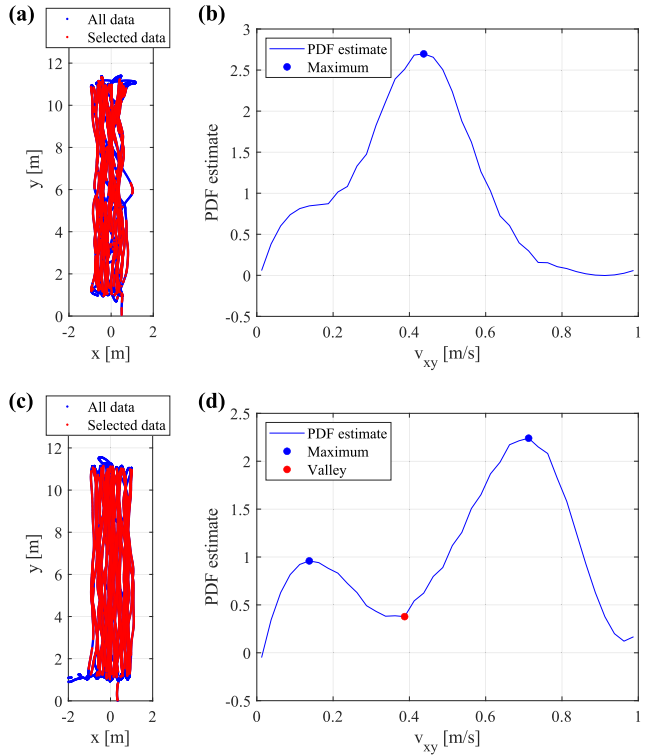


**FIGURE 6.** Analysis of the UAV flight path as a function of the along-track flight speed. Flight speed of 50 cm/s: flight path and measurement positions (a), probability density function of the UAV speed on the XY plane ( $v_{xy}$ ) (b). Flight speed of 75 cm/s: flight path and measurement positions (c), probability density function of the UAV speed on the XY plane ( $v_{xy}$ ) (d).

radar, and the central antenna is connected to the transmitter. Thus, the spacing between the receiving antennas is 19.6 cm. This distance is taken into account to correct the phaseshift due to the different position of the receiving antennas. In addition to this, a calibration stage using a reference metallic disk placed on the soil has been conducted. This calibration stage is needed to estimate the value of a phaseshift ( $\Delta\phi$ ) that has to be introduced between channels 1 and 2 to ensure that the reflection on the metallic disk observed in each individual SAR image is in-phase, so that these reflections are combined constructively.

## IV. RESULTS

### A. DESCRIPTION OF THE SCENARIO

The improved UAV-based GPR system for IEDs and landmine detection has been validated at the airfield for UAVs of the Technical School of Engineering of Gijón, located at coordinates (43.522, -5.624). Two people are required to conduct the measurements: one is the responsible of the ground station (laptop), being in charge of configuring the different subsystems described in Section II-A. This person also supervises that the system is working as expected. The other person manages the radio-control unit of the UAV for manual flight mode (required for takeoff and landing). Concerning the time required for the preparation of the prototype, thanks to the

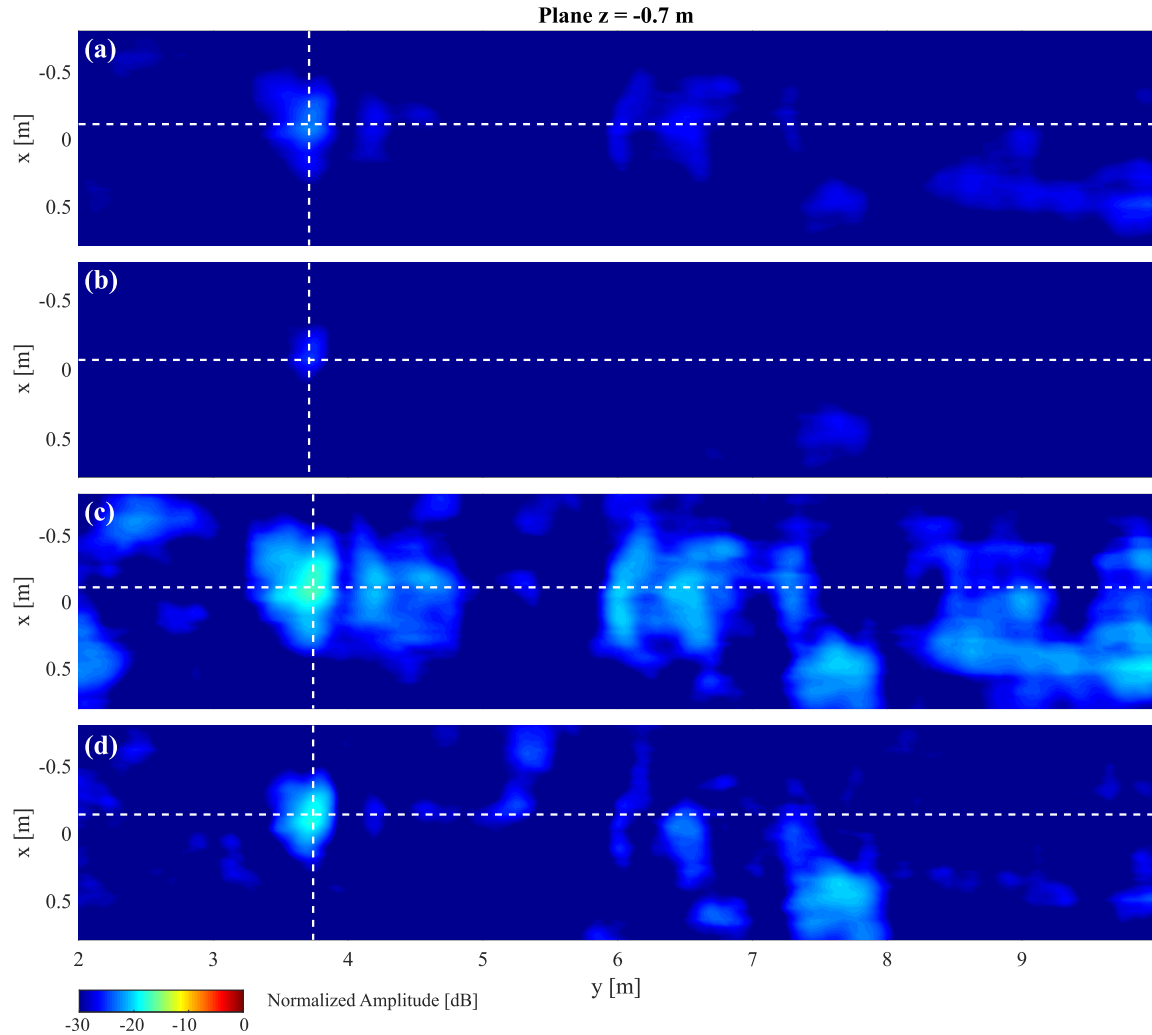


**FIGURE 7.** SAR image. Horizontal cut  $z = -70$  cm centered at the location of the 18 cm diameter metallic disk buried 25 cm deep. Normalized reflectivity, in dB. Coherent combination of Rx channels 1 and 2. Without applying SVD filtering nor processing gain (a), applying SVD filtering (b), applying processing gain (c), applying SVD filtering and processing gain (d).

use of a dual-band GNSS-RTK receiver, maximum positioning accuracy is achieved within seconds after powering the UAV up. In other systems equipped with single-band GNSS-RTK modules [31], reaching the maximum accuracy can take several minutes.

A picture of the scenario is shown in Fig. 5 together with an scheme of the flight path followed by the UAV (Fig. 5, left).

The soil of the area-under-test is a loamy soil with a high degree of moisture, since a hygrometer measures a 40-60% of water vapor when placed inside this soil. The relative permittivity of the soil is within  $\varepsilon_r = 5$  and  $\varepsilon_r = 8$ , which is in agreement with the expected relative permittivity values for loamy soils. As shown in Fig. 5, two targets have been buried: the first one is a metallic disk, buried at 25 cm depth, and the second is an anti-personnel plastic landmine, buried at 13 cm depth. The coordinates of these targets in the local coordinate system are indicated in Fig. 5.

Given the working frequency band (from  $f_{min} = 600$  MHz to  $f_{max} = 3$  GHz), theoretical range resolution is  $\Delta R_z = 6.3$  cm in free-space. Concerning cross-range resolution, a mask of size  $M_x = 1$  m  $\times$   $M_y = 2$  m is considered when applying SAR processing. This means that the reflectivity on each voxel is computed considering the measurements contained in a rectangle of size  $M_x \times M_y$  centered on such voxel. The choice of this mask is based on the estimation of the along-track and across-track coherence lengths. The former has been selected based on the analysis shown in [31] for different coherence lengths and their impact in the SAR images. Across-track coherence length is shorter than along-track coherence length (1 m instead of 2 m) because geo-referred uncertainties are more correlated within the same sweep (along-track acquisition). Therefore, cross-range resolution (at the air-soil interface,  $h = 2.3$  m) is  $\Delta R_x = \lambda h / M_x = 38.3$  cm,  $\Delta R_y = \lambda h / M_y = 19.2$  cm.

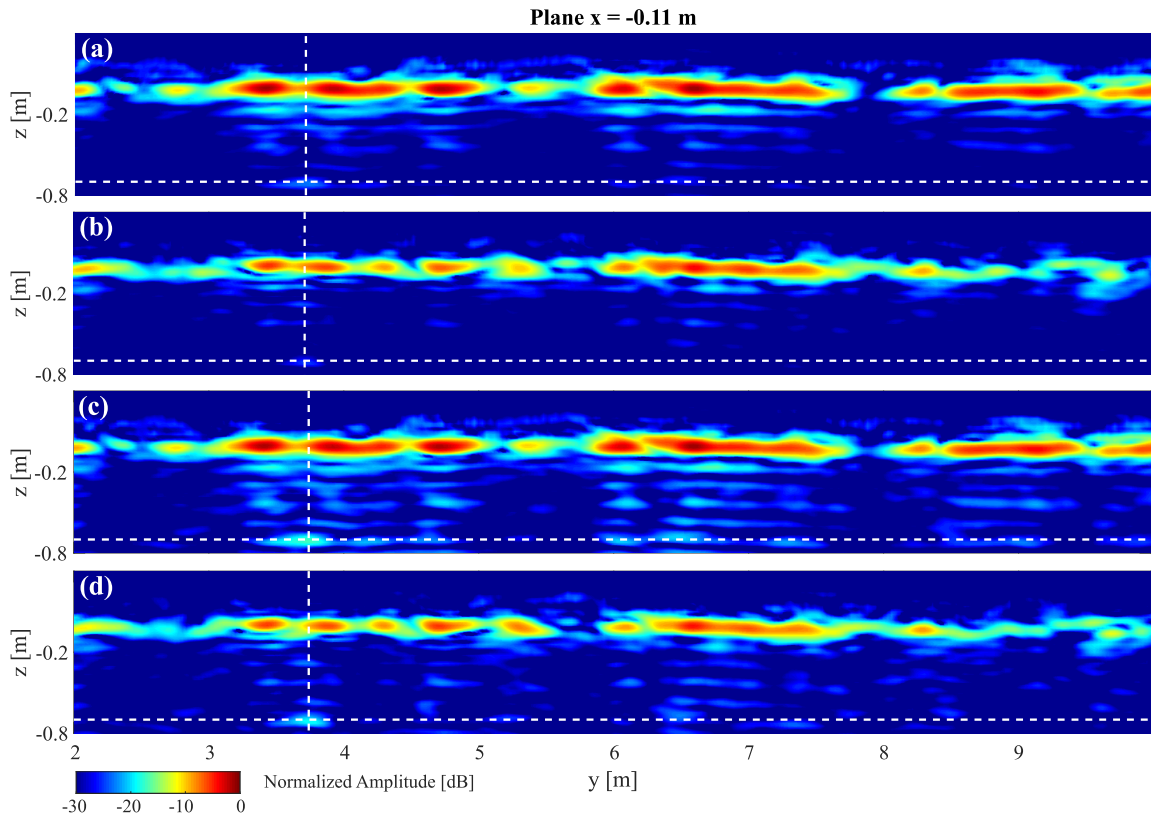


**FIGURE 8.** SAR image. Vertical along-track cut  $x = -11$  cm centered at the location of the 18 cm diameter metallic disk buried 25 cm deep. Normalized reflectivity, in dB. Coherent combination of Rx channels 1 and 2. Without applying SVD filtering nor processing gain (a), applying SVD filtering (b), applying processing gain (c), applying SVD filtering and processing gain (d).

As explained in [32], the investigation domain is shrunk in the  $XY$  plane with respect to the acquisition domain to avoid edge effects in the GPR-SAR images. Thus, an investigation domain of size  $L_{x'} = 1.6$  m and  $L_y = 8$  m has been considered (as shown in Fig. 4). This is 0.8 times the size of the acquisition domain (along both  $x$  and  $y$  axes).

#### B. UAV SCAN SPEED ANALYSIS

The flight path is defined as follows: first, the area to be scanned is defined using a Geographic Information System (GIS) tool and then, the separation between waypoints in the  $x$  and  $y$  axes is selected to obtain the waypoints. Once the waypoints are set, they are loaded into the UAV flight controller. After the takeoff procedure, the UAV flies autonomously following the pre-defined path based on the waypoints. The heading of the UAV is kept fixed to the same value (in particular, fixed to the desired course over ground) during the entire flight, so that the UAV does not rotate 180° after reaching the end of a sweep. Instead, it flies forward and backward alternatively. Thanks to this, course and attitude are kept stable during the entire flight, resulting in a better GPR-SAR image. Besides, 180° turns would result in sharp flight oscillations that could impact the equipment on board the UAV, apart from limiting the flight time. It is worth noting that radar measurements are continuously gathered during the whole

flight. A video illustrating how scanning is performed can be watched at: <https://youtu.be/HDUwgka8Dns>.

As shown in Fig. 5, the area scanned with the prototype has a size of  $L_y = 10$  m (along-track direction,  $y$  axis)  $\times L_x = 2$  m (across-track direction,  $x$  axis), being 6 cm the spacing between two consecutive along-track sweeps. This results in 34 along-track sweeps (17 forward and 17 backward), so that the overall flight path length is 342 m. As the time required to complete the flight path defined with waypoints is around 12 minutes, the average flight speed is around 47 cm/s. The flight speed on each along-track scan is faster since it has been set to 75 cm/s. The reason why the average speed is smaller is because after finishing each along-track sweep the UAV has to slow down, perform a lateral displacement of 6 cm, and then increase the speed until reaching again the along-track speed of 75 cm/s.

UAV flight speed also impacts the smoothness of the UAV flight path. To analyze this parameter, two scans of the area-under-test have been conducted at different flight speeds. Results are shown in Fig. 6 (a),(b) for an along-track flight speed of 50 cm/s, and in Fig. 6 (c),(d) for an along-track flight speed of 75 cm/s. It can be noticed that flying at slower speed results in less straight along-track trajectories when comparing Fig. 6 (a) and Fig. 6 (c). It is consistent with the fact that the momentum of the UAV ( $\text{mass} \times \text{speed}$ ) is smaller

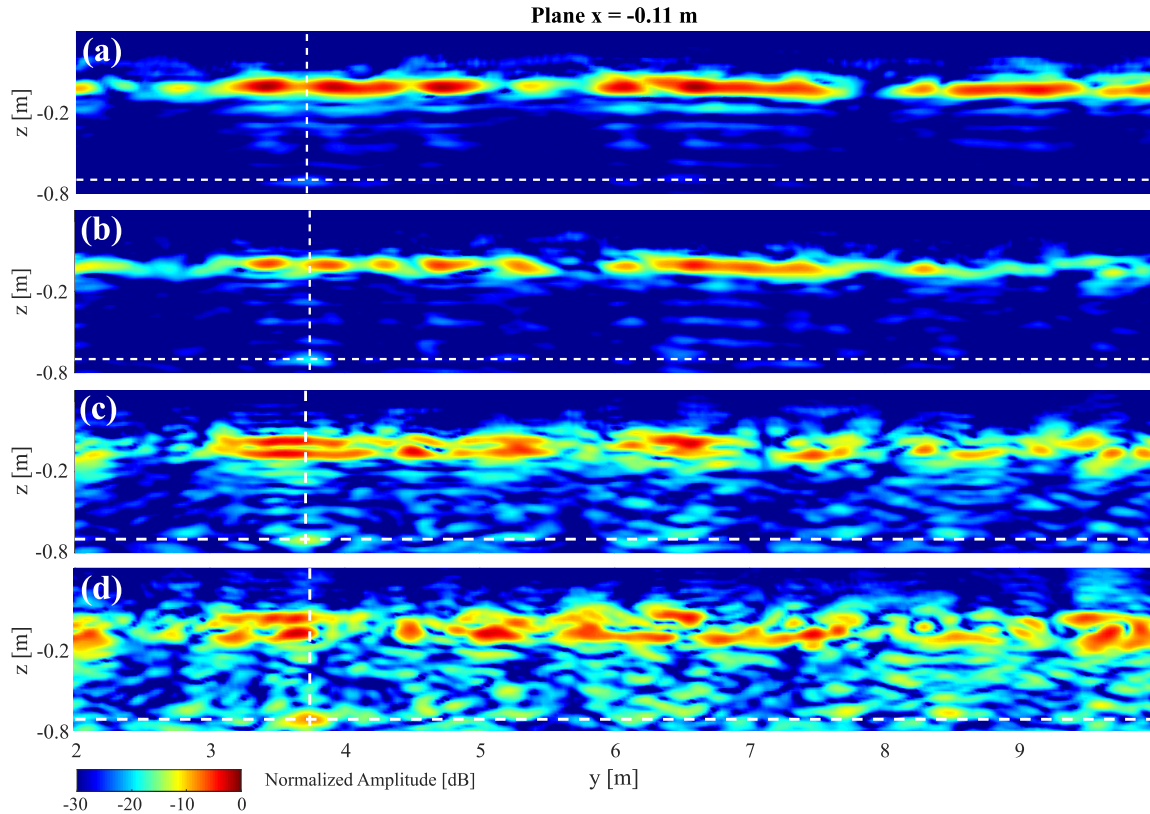


**FIGURE 9.** SAR image. Vertical along-track cut  $x = -11$  cm centered at the location of the 18 cm diameter metallic disk buried 25 cm deep. Normalized reflectivity, in dB. Coherent combination of Rx channels 1 and 2. Processing gain is applied. No SVD filtering (a), SVD filtering: first eigenimage removed (b), first and second eigenimages removed (c), four first eigenimages removed (d).

at slower speeds, so lateral forces (e.g. wind, the proper feedback of the propellers to follow the waypoints) have more impact in the UAV flight path.

Fig. 6 (b) and Fig. 6 (d) show the histogram of the UAV flight speed when the area-under-test is scanned. At higher speed (Fig. 6 (d)) two peaks can be identified, the highest corresponding to the UAV along-track speed (75 cm/s), and the smallest corresponding to lateral displacements from one along-track scan to the next one. The speed profile/histogram can be used to filter out positioning and radar measurements (as introduced in [38]), selecting only the data corresponding to UAV flight speeds above a certain threshold, which corresponds to along-track acquisition (e.g. speed greater than 40 cm/s in the case of Fig. 6 (d)). In the case of Fig. 6 (b), it is more difficult to filter the positions corresponding to along-track acquisitions using the speed profile information, as there is not a distinctive separation between low-speed operations and the along-track flight speed of 50 cm/s. Finally, it must be remarked that higher flight speeds result in larger areas to be scanned. Thus, results presented hereinafter correspond to an along-track flight speed operation of 75 cm/s (except for one case shown to illustrate the impact of the flight path smoothness in the SAR images). Although faster speeds could be achieved with the implemented prototype, it has been decided to keep the operation speed below 100 cm/s for safety reasons.

Concerning the size of the area that can be scanned in a single flight using the improved prototype, it must be pointed out that it is within the size of the search lanes defined in Section 4.1 of [39] suggested for demining procedures.

### C. GPR-SAR RESULTS

The following subsection shows GPR-SAR results for the radar measurements collected during the flight whose path is shown in Fig. 6 (c). Results for the metallic disk will be analyzed first, considering the improvements explained in Section III. It must be mentioned that free-space propagation is considered in the GPR-SAR algorithm ( $\varepsilon_r = 1$ ), so the echo corresponding to the reflection on the buried targets will appear deeper than the true position of the targets.

Fig. 7 (a) and Fig. 8 (a) show the SAR image cuts centered at the location of the metallic disk when the SAR images of both receiving channels are coherently combined, but before applying SVD filtering and processing gain. It can be noticed that the amplitude of the reflection on the metallic disk is 25 dB below the amplitude of the air-soil interface (located at  $z = 0$  cm), and only around 5 dB above the ground/clutter level.

Next, results when SVD filtering is introduced in the radar measurements processing are depicted in Fig. 7 (b) and Fig. 8 (b): a reduction in the clutter can be noticed, together with

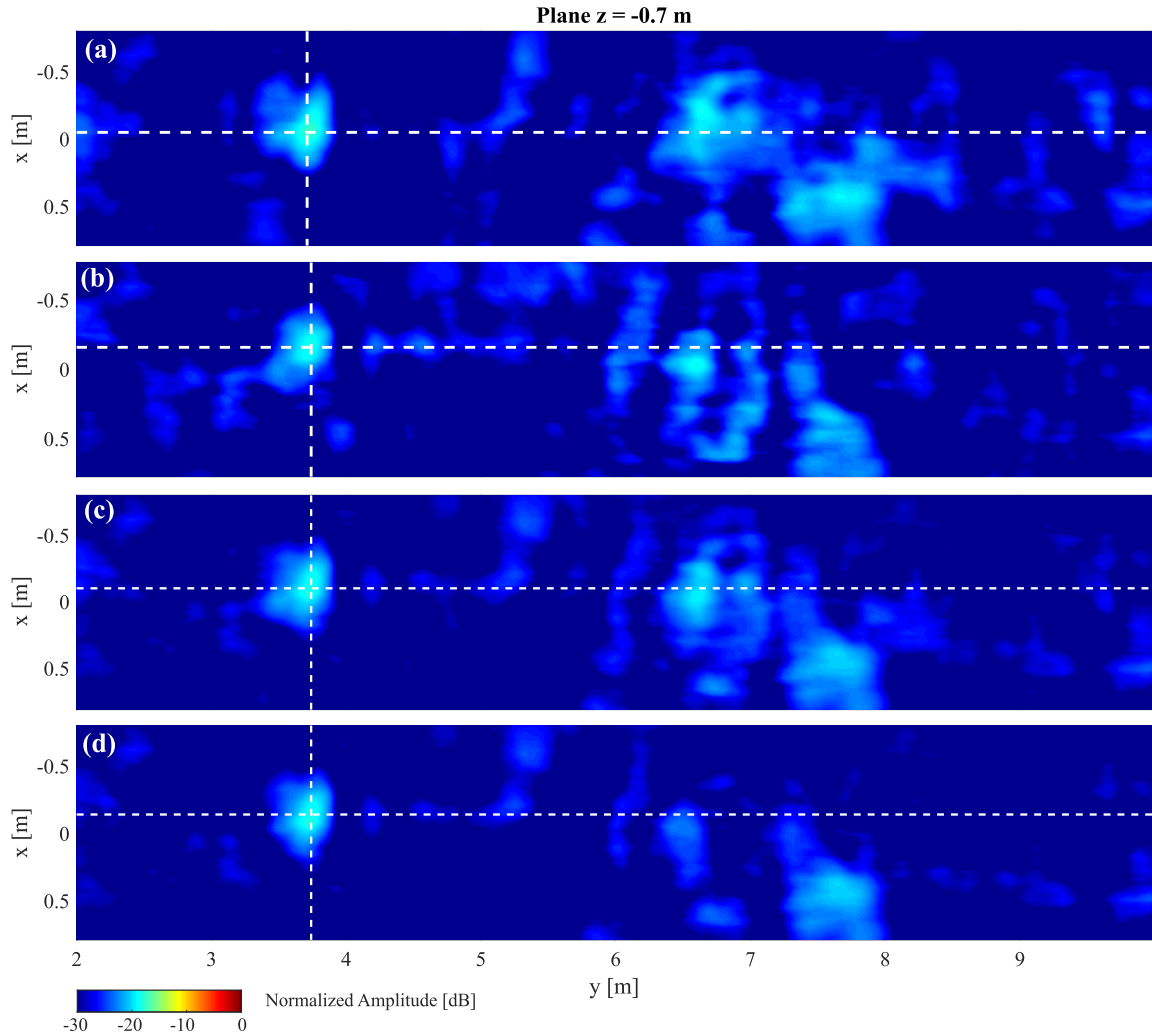


**FIGURE 10.** SAR image. Horizontal cut  $z = -70$  cm centered at the location of the 18 cm diameter metallic disk buried 25 cm. Normalized reflectivity, in dB. Rx channel 1 (a), Rx channel 2 (b), incoherent combination of Rx channels 1 and 2 (c), and coherent combination of Rx channels 1 and 2 (d). SVD filtering and processing gain is applied.

the partial filtering of the reflection at the air-soil interface (Fig. 8 (b)). Fig. 7 (c) and Fig. 8 (c) show the effect of applying processing gain: the level of the reflection on the metallic disk is increased in around 6-7 dB, but also the clutter. Finally, the combination of SVD filtering and processing gain is plotted in Fig. 7 (d) and Fig. 8 (d), where the reflection on the metallic disk is enhanced due to the processing gain contribution and the clutter is significantly reduced thanks to the SVD filtering. Apart from the reflection on the metallic disk, another artifact located at  $x = 0.5$  m and  $y = 7.5$  is observed, which could be caused by the soil inhomogeneity (a wetter area or a stone).

As explained in Section III-A, SVD filtering is based on removing the first eigenimage, associated to the highest singular value,  $\sigma_1$ . To justify why this conservative procedure has been adopted, SAR image cuts when different eigenimages are removed are shown in Fig. 9. Results depicted in Fig. 9 (b)-(d) correspond to the cases where one, two, and four eigenimages are removed (associated to the highest

singular values), whereas Fig. 9 (a) corresponds to the case where SVD filtering is not applied. It can be noticed that the clutter level increases as more eigenimages (associated to the highest correlated information, such as air-soil reflections) are removed.

Concerning the depth at which the echo is located, it is 70 cm below the air-soil reflection. As the true depth is 25 cm, the soil permittivity can be estimated as  $\varepsilon_r = (70/25)^2 = 7.8$ , which is within the range of the expected relative permittivity for a loamy soil ( $\varepsilon_r = 5$  to 8).

As stated in Section III-B, the goal behind the coherent combination of the two receiving channels is to reduce the clutter, as well as increasing the scanned area per unit of time. The former is due to the fact that clutter appearing in the SAR images created using only the measurements of one receiving channel is likely to cancel partially or totally when the SAR images of both channels are added coherently. Hence, the reflectivity values corresponding to reflections at buried targets would be reinforced. Results of the SAR

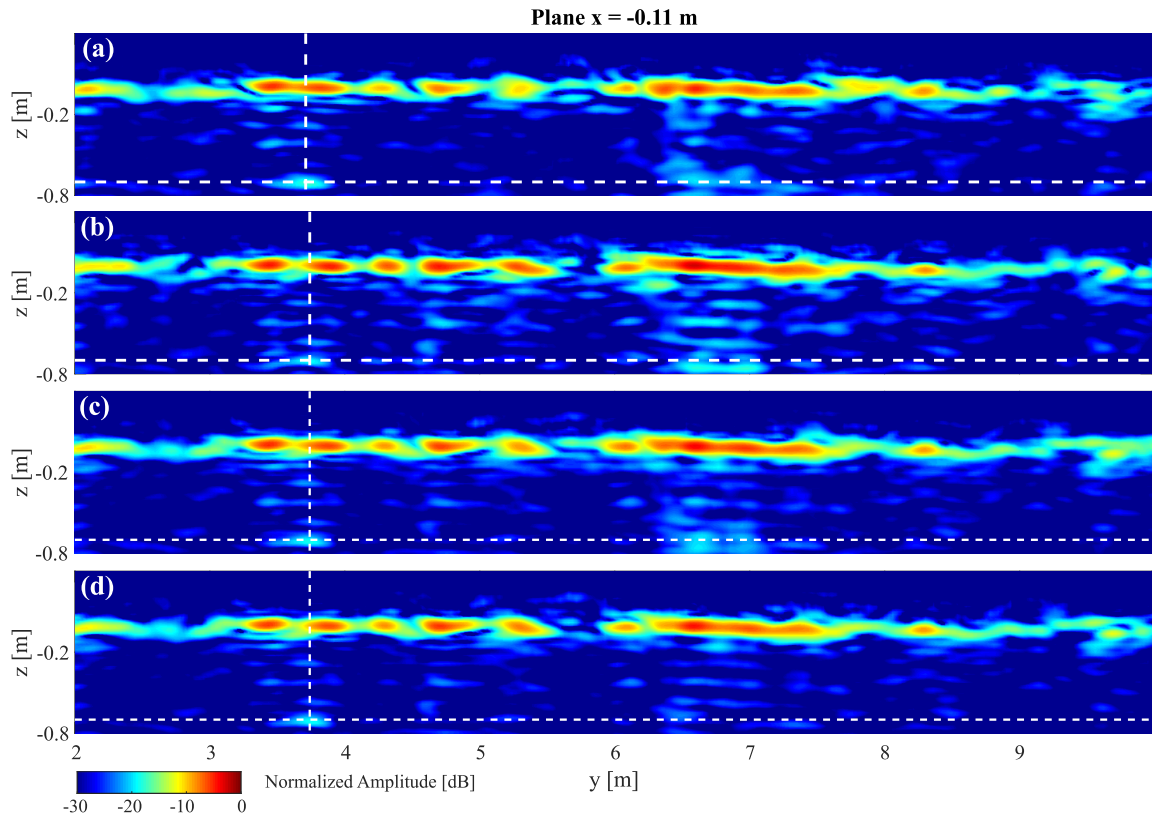


**FIGURE 11.** SAR image. Vertical along-track cut  $x = -11$  cm centered at the location of the 18 cm diameter metallic disk buried 25 cm. Normalized reflectivity, in dB. Rx channel 1 (a), Rx channel 2 (b), incoherent combination of Rx channels 1 and 2 (c), and coherent combination of Rx channels 1 and 2 (d). SVD filtering and processing gain is applied.

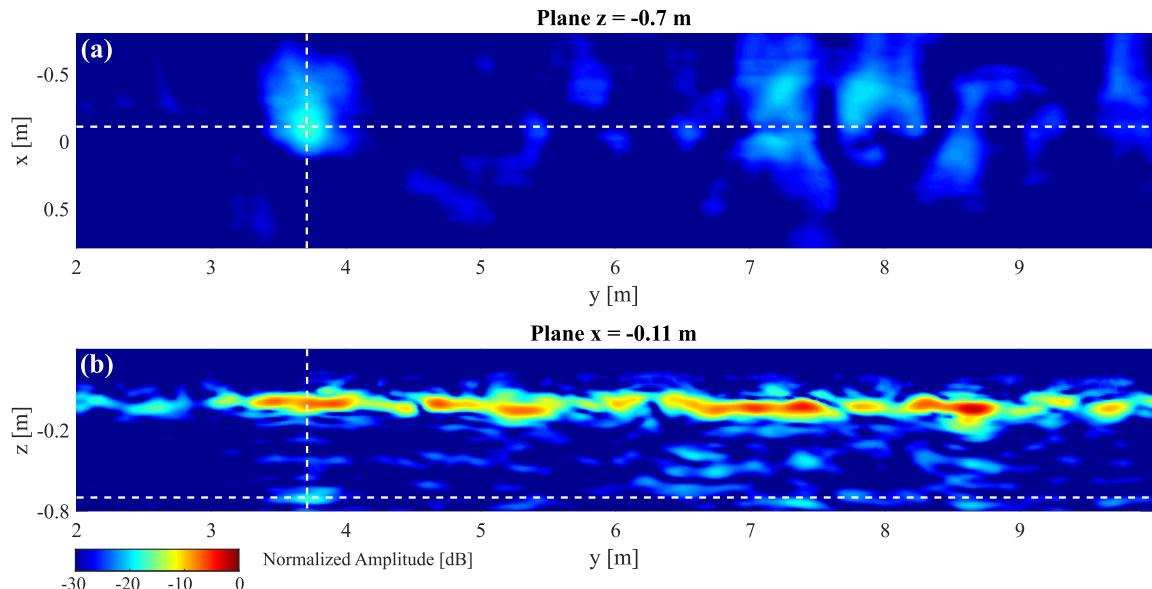


**FIGURE 12.** SAR image when along-track flight speed is 50 cm/s. Cuts  $z = -70$  cm (a) and  $x = -11$  cm (b) centered at the location of the 18 cm diameter metallic disk buried 25 cm. Normalized reflectivity, in dB. Coherent combination of Rx channels 1 and 2, applying SVD filtering and processing gain.

images are shown in Fig. 10 (a) and Fig. 11 (a) for channel 1, and in Fig. 10 (b) and Fig. 11 (b) for channel 2. Horizontal and vertical cuts of the SAR image corresponding to the

incoherent (power) combination of the SAR images of the two receiving channels are depicted in Fig. 10 (c) and Fig. 11 (c). For comparison purposes, results corresponding

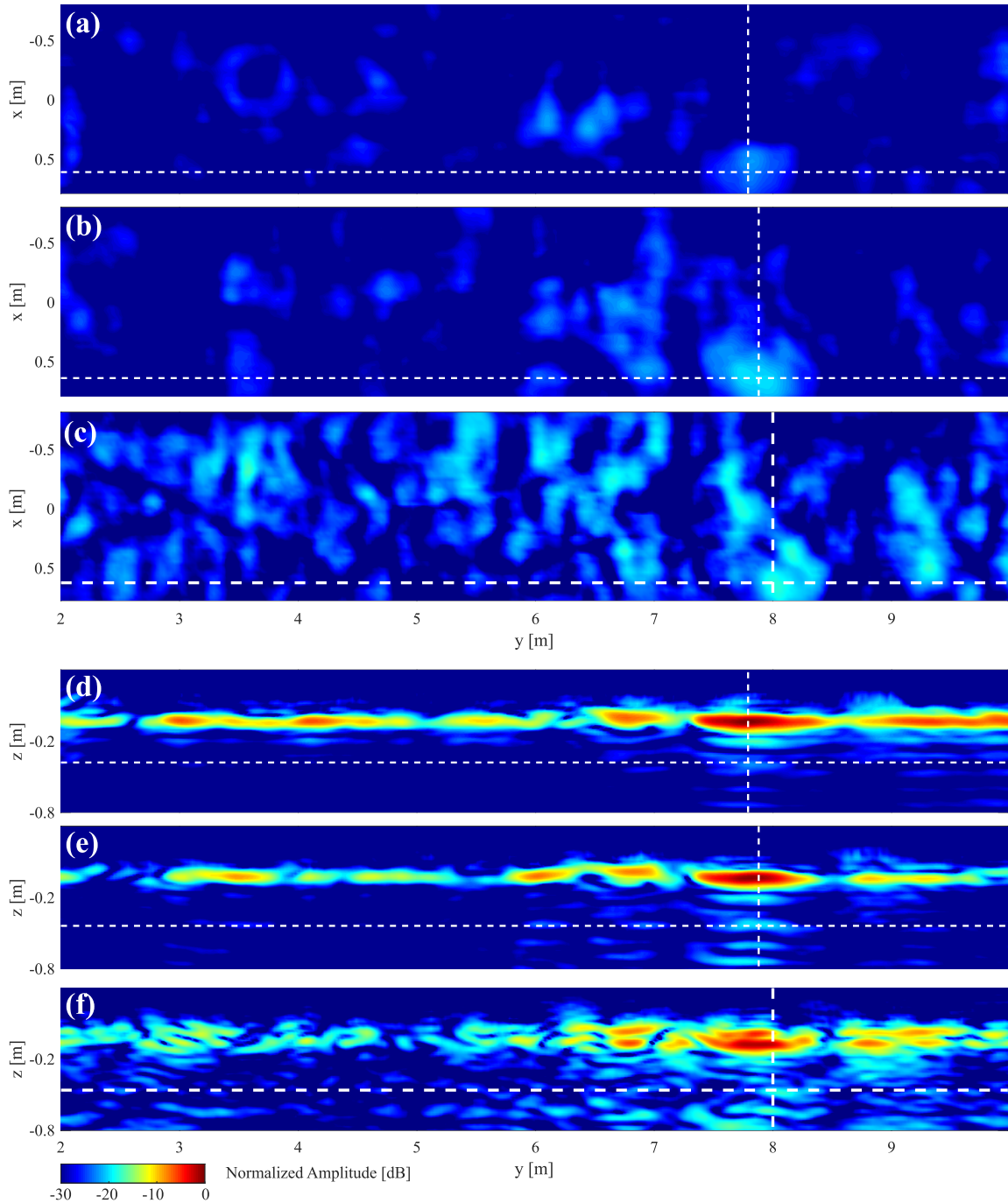


**FIGURE 13.** SAR image. Cuts centered at the location of the 16 cm diameter anti-personnel plastic landmine buried 13 cm. Normalized reflectivity, in dB. Coherent combination of Rx channels 1 and 2. Without applying processing gain nor SVD filtering: cut  $z = -38$  cm (a) and  $x = 61$  cm (d). Applying processing gain and SVD filtering (first eigenimage removed): cut  $z = -44$  cm (b) and  $x = 64$  cm (e). Applying processing gain and SVD filtering (first and second eigenimages removed): cut  $z = -46$  cm (c) and  $x = 64$  cm (f).

to the coherent combination of both channels are shown in Fig. 10 (d) and Fig. 11 (d). Clutter at  $x = 0.5$  m and  $y = 7.5$  m is present in the four compared cuts (at  $z = -70$  cm and  $x = -5$  cm), but clutter around  $x = 0$  m and  $y = 6.5$  m disappears when coherent combination is applied. Thus, the former artifact observed in the SAR images could denote the presence of another object (e.g. a

stone) or a wetter area of the soil. Concerning the detectability of the metallic disk, the amplitude of the reflectivity of the metallic disk is almost the same in the four compared results (around -18 dB).

The impact of the flight smoothness in the SAR images is also analyzed by processing the measurements collected during the flight conducted at an along-track flight speed

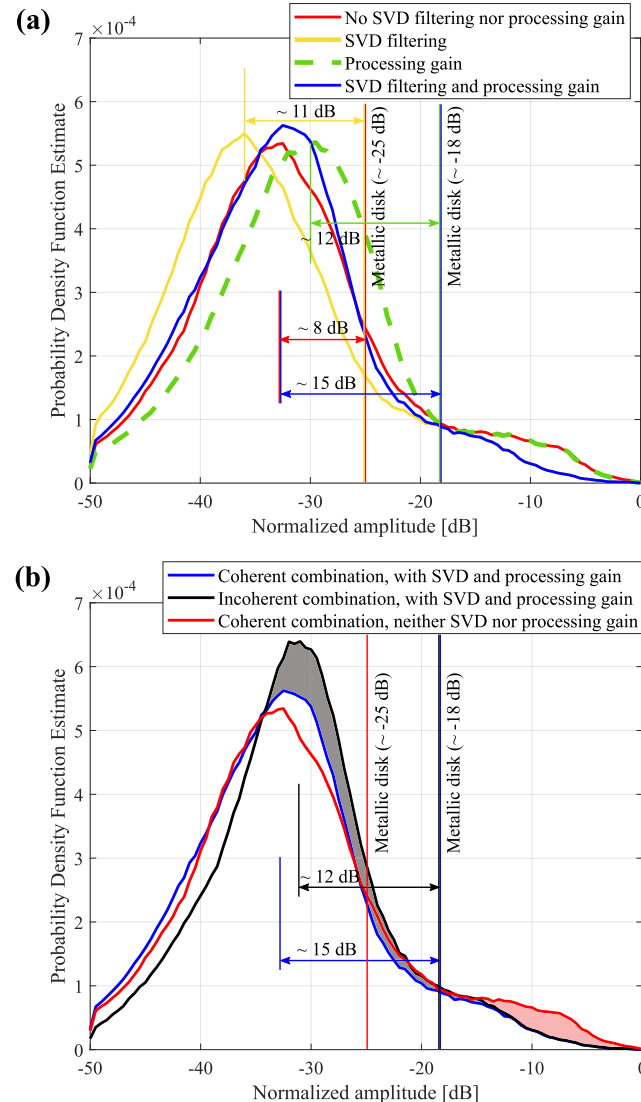


**FIGURE 14.** Probability density function of the reflectivity within the investigation domain. Comparison of the impact of SVD filtering and processing gain (a). Comparison of coherent and incoherent combination of the SAR images associated to each receiving channel of the radar module (b). Vertical lines represent the reflectivity of the buried metallic disk for each analyzed case.

of 50 cm/s (Fig. 6 (a,b)). SAR results are shown in Fig. 12, applying the same processing and improvements as in Fig. 7 (d) and Fig. 8 (d). If both figures are compared, it can be observed that results from the flight at 50 cm/s exhibit higher clutter, especially within the area corresponding to  $y = 7$  m to  $y = 8.5$  m. The presence of more clutter can be due to the fact that, as the acquisition positions are less uniformly spaced, gaps greater than half-a-wavelength (5 cm at the highest frequency) may occur. This results in partial aliasing, observed in the SAR image as clutter.

SAR images corresponding to the horizontal and vertical cuts centered at the location of the anti-personnel plastic landmine are shown in Fig. 13. The coherent combination of the two receiving channels is applied for obtaining these

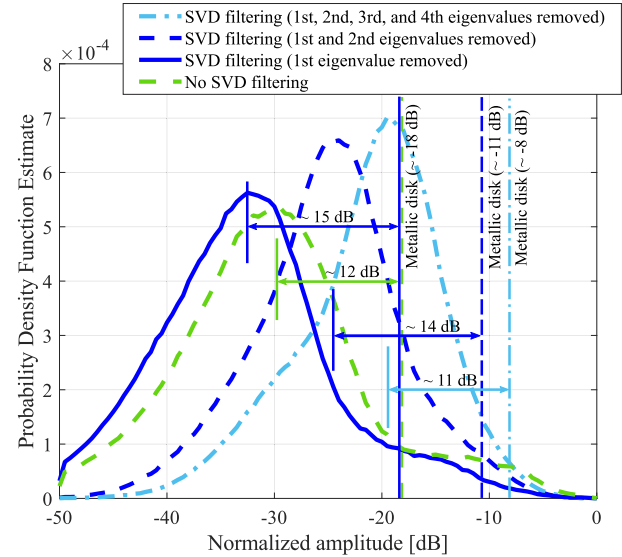


**FIGURE 15.** Probability density function of the reflectivity within the investigation domain. Comparison of the impact of SVD filtering when different number of eigenimages are removed. Vertical lines represent the reflectivity of the buried metallic disk for each analyzed case.

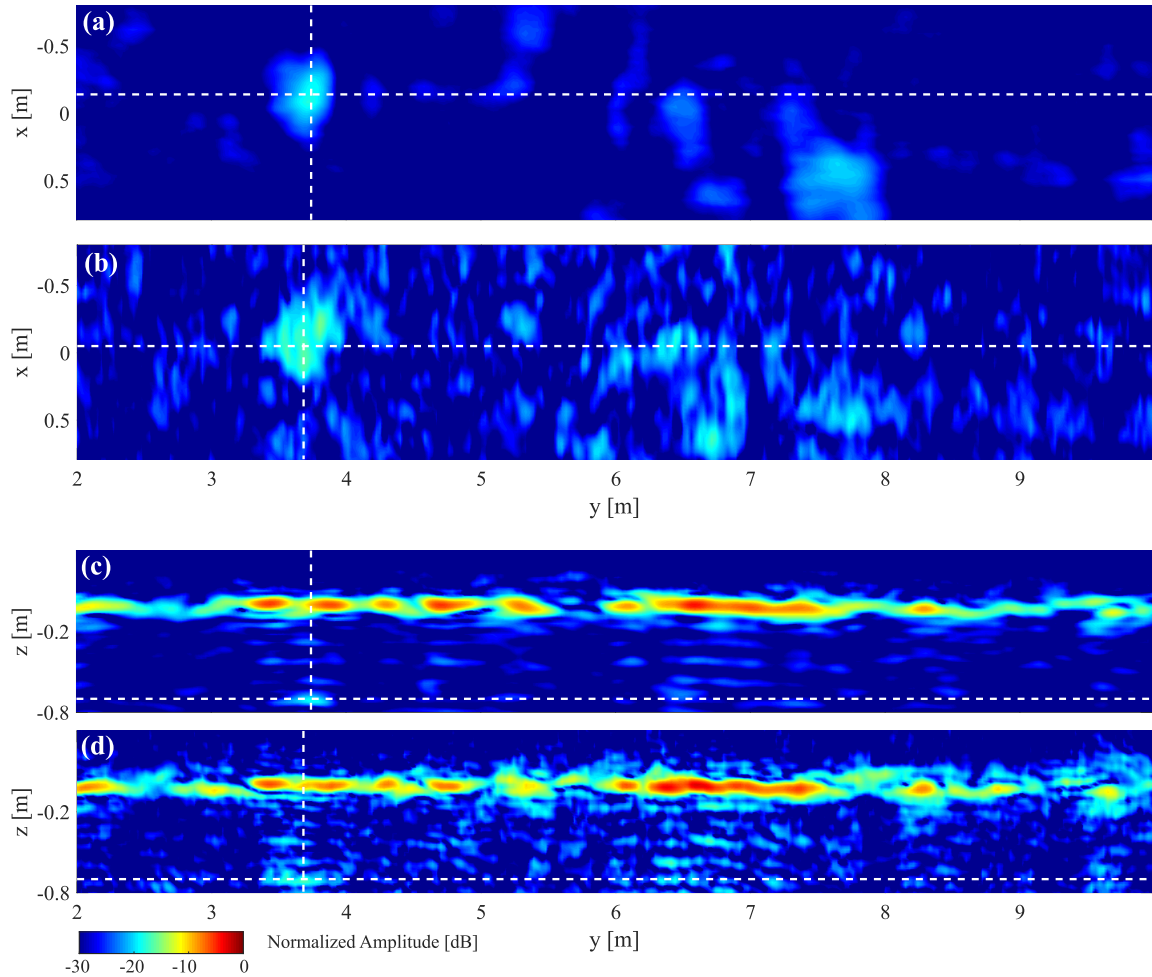
results. Fig. 13 (a,d) corresponds to the cases where neither SVD filtering nor processing gain are applied, whereas the results after considering these improvements are shown in Fig. 13 (b,e). As in the case of the metallic disk (Fig. 7 and Fig. 8), the amplitude of the reflectivity corresponding to the plastic landmine is increased by 6-7 dB, without observing a significant impact in the clutter. In the case of Fig. 13 (e) the interface between the soil and the plastic landmine is detected at a depth of  $z = -44$  cm. Besides, another reflection happening 15 cm deeper can be also observed. This echo can be the reflection from the lower face of the plastic landmine, that is, from the interface between the base of the plastic landmine and the soil. The plastic landmine is 8 cm thick, so its relative permittivity ( $\epsilon_{r,PLM}$ ) can be estimated as follows:  $\epsilon_{r,PLM} = (15/8)^2 = 3.5$ .

Fig. 13 (c,f) corresponds to the case where the first and second eigenimages are removed when SVD filtering is applied. Similarly to the results depicted in Fig. 9, removing more eigenimages increases the clutter of the SAR image.

#### D. QUANTITATIVE ANALYSIS

In order to quantify the improvements introduced in this contribution (the coherent combination of the receiving channels and the application of SVD filtering and processing gain), the probability density function of the SAR image normalized amplitude is computed [32]. Results are shown in Fig. 14.

First, the impact of SVD filtering and processing gain is shown in Fig. 14 (a), considering the coherent combination of the SAR images for each receiving channel. The reflectivity of the metallic disk according to the levels observed in Fig. 7 and Fig. 8 are indicated in the figure with vertical lines. The peak of the probability density function corresponds to the clutter level of the SAR image, so the Signal-to-Clutter Ratio



**FIGURE 16.** SAR image. Cuts  $z = -70$  cm (a,b) and  $x = -11$  cm (c,d) centered at the location of the 18 cm diameter metallic disk buried 25 cm deep. Normalized reflectivity, in dB. Coherent combination of Rx channels 1 and 2, applying SVD filtering and processing gain. Considering a mask of size  $M_x \times M_y$  to compute the reflectivity on each voxel (a,c), and considering the entire acquisition domain ( $L_x \times L_y$ ) to compute the reflectivity on each voxel (b,d).

can be estimated as the difference between the amplitude of the target (in this example, the metallic disk) and the peak of the probability density function.

The red line corresponds to the case where no processing improvements are introduced, noticing that the Signal-to-Clutter Ratio is around 8 dB (the reflectivity level of the metallic disk is around  $-25$  dB). When SVD filtering is introduced (yellow line), the reflectivity level of the metallic disk remains at  $-25$  dB, but the clutter is reduced, thus resulting in an improvement of 3 dB in the Signal-to-Clutter Ratio. Besides, the level of the probability density function between  $-15$  dB and  $-3$  dB decreases (Fig. 14 (b), area shaded in red) as part of the reflection at the air-soil interface is also filtered. When processing gain is applied (dashed green line), both the amplitude of the reflection on the target and the clutter increase, but at a different rate (reflectivity of the metallic disk increases from  $-25$  dB to  $-18$  dB, and clutter from  $-33$  dB to  $-30$  dB). Thus, processing gain improves the Signal-to-Clutter Ratio in around 3-4 dB, similarly to SVD filtering.

Finally, the blue line shows the combination of processing gain and SVD filtering. It can be noticed that the clutter is similar to the case where no improvements were introduced (red line). However, as the amplitude of the reflection on the target has been improved by means of the processing gain, the resulting Signal-to-Clutter Ratio when combining SVD filtering and processing gain increases until 15 dB.

Quantitative analysis of the impact of the coherent combination of the SAR images is analyzed in Fig. 14 (b). The black line corresponds to incoherent combination of the receiving channels when SVD filtering and processing gain are applied (Fig. 10 (c) and Fig. 11 (c)), and the blue line corresponds to the coherent combination of the receiving channels when SVD filtering and processing gain are applied (Fig. 10 (d) and Fig. 11 (d)). If the incoherent and coherent combinations are compared, it can be noticed that, whereas the reflectivity of the metallic disk does not change significantly, the peak of the clutter decreases around 2-3 dB when coherent combination is considered. This reduction in the amplitude of the clutter

corresponds to the area shadowed in gray color in Fig. 14 (b), and supports the fact that the coherent combination of two SAR images contributes to mitigate the clutter. The impact in the Signal-to-Clutter Ratio is an increase of around 3 dB.

Next, the probability density function when different number of eigenimages are removed is plotted in Fig. 15 to quantify the SVD analysis depicted in Fig. 9. It can be observed that the Signal-to-Clutter Ratio decreases when more eigenimages are removed, achieving the maximum when only the first eigenimage is removed.

#### E. EFFECT OF MASKING THE ACQUISITION DOMAIN

As explained in Section III-B, to compute the reflectivity on each voxel of the investigation domain, only the radar measurements within a mask of size  $M_x = 1 \text{ m} \times M_y = 2 \text{ m}$  centered at the  $x'$ ,  $y'$  coordinates of the voxel were considered. This mask defines the amount of measurements that are coherently combined to form the SAR image, and its size is defined from the estimation of the coherence length along  $x$  and  $y$  axes.

The impact of considering a reduced set of measurements to calculate the reflectivity on each voxel with respect to the use of all the measurements within the acquisition domain is assessed in Fig. 16. In this figure, the SAR images at the horizontal and vertical cuts centered at the metallic disk are compared with and without applying masking. It could be expected that the use of all the measurements to compute the reflectivity on each voxel would result in better resolution (as the synthetic aperture size would be  $L_x \times L_y$  instead of  $M_x \times M_y$ ). However, the reality is that the resulting SAR images (Fig. 16 (b,d)) exhibit more clutter and even worse cross-range resolution. Cumulative geo-referring errors cause that position uncertainties between the first and last acquisitions are likely to be greater than the required uncertainty to apply SAR processing (around 1/10 of the wavelength).

#### V. CONCLUSION

An improved UAV-based GPR system for the safe detection of IEDs and landmines has been presented. Some of the improvements have been done in the area of radar data pre-processing, by means of SVD filtering and processing gain. The former reduces the clutter due to the reflection of the signal in the air-soil interface, and the latter improves the Signal-to-Clutter Ratio within a particular depth range, thus allowing better detection capabilities. Besides, the use of a dual-channel receiver contributes to clutter reduction by performing the coherent combination of the SAR images obtained for each channel. As shown in the results, when applying together SVD filtering, processing gain and coherent combination, the Signal-to-Clutter Ratio is improved around 7 dB (from 8 dB to 15 dB). Finally, the employment of masks for computing the SAR images also contributes to mitigate the clutter and to improve the target discrimination.

Compared to the previous version of the system, [32], the SAR imaging area (investigation domain) has been increased from  $1 \text{ m} \times 4 \text{ m}$  to  $1.6 \text{ m} \times 8 \text{ m}$  (across-track

and along-track dimensions respectively). This means that the scanning capabilities have been increased by a factor of 3 thanks to the improvements described in this contributions while maintaining the same UAV platform and batteries.

It is worth noting that, although this UAV-based GPR system is primarily devoted to detect explosives such as antipersonnel landmines, it can also be used for other non-destructive testing GPR applications, such as the detection of buried civil infrastructure.

Finally, a video summarizing the improvements and results presented in this contribution can be watched at: <https://youtu.be/8y-raqTZqxAw>.

#### ACKNOWLEDGMENT

The authors would like to thank D. C. Martínez and A. D. Mitri for their help and support with the UAV flight preparation at the airfield of the University of Oviedo. The authors would like to acknowledge Cap. Santiago García Ramos and the CIED-COE (Col. José Luis Mingote Abad) for the supervision of the Contract 2019/SP03390102/00000204/CN-19-002 (“SAFEDRONE”) and for the technical suggestions concerning the preparation of the tests.

#### REFERENCES

- [1] H. Hold, *Ground Penetrating Radar: Theory Application*. Amsterdam, The Netherlands: Elsevier Science, 2008.
- [2] A. H. Trang and H. G. Irion, “Simulation of close-in and stand-off mine detection,” in *Proc. IEEE Int. Geosci. Remote Sens. Symp.*, Dec. 1997, pp. 1132–1134.
- [3] G. Liu, Y. Wang, J. Li, and M. R. Bradley, “SAR imaging for a forward-looking GPR system,” in *Proc. Detection Remediation Technol. Mines Minelike Targets*, Sep. 2003, pp. 322–333.
- [4] E. M. Rosen and E. Ayers, “Assessment of down-looking GPR sensors for landmine detection,” in *Proc. Detection Remediation Technol. Mines Minelike Targets*, Jun. 2005, pp. 423–434.
- [5] A. M. Zoubir, I. J. Chant, C. L. Brown, B. Barkat, and C. Abeynayake, “Signal processing techniques for landmine detection using impulse ground penetrating radar,” *IEEE Sensors J.*, vol. 2, no. 1, pp. 41–51, 2002.
- [6] D. J. Daniels, “A review of GPR for landmine detection,” *Sens. Imag., Int. J.*, vol. 7, no. 3, pp. 90–123, Sep. 2006.
- [7] Y. Fuse, “A novel forward and backward scattering wave measurement system for optimizing GPR standoff mine/IED detector,” in *Proc. Detection Sens. Mines, Explosive Objects, Obscured Targets*, May 2012, p. 835.
- [8] M. A. Gonzalez-Huici and F. Giovannesci, “A combined strategy for landmine detection and identification using synthetic GPR responses,” *J. Appl. Geophys.*, vol. 99, pp. 154–165, Dec. 2013.
- [9] A. M. Cunliffe, R. E. Brazier, and K. Anderson, “Ultra-fine grain landscape-scale quantification of dryland vegetation structure with drone-acquired structure-from-motion photogrammetry,” *Remote Sens. Environ.*, vol. 183, pp. 129–143, Sep. 2016.
- [10] J. Sungwook, H. Cho, K. Donghoon, K. Kyukwang, J.-I. Han, and H. Myung, “Development of algal Bloom removal system using unmanned aerial vehicle and surface vehicle,” *IEEE Access*, vol. 4, pp. 1148–1162, 2016.
- [11] A. Bhardwaj, L. Sam, Akansha, F. J. Martin-Torres, and R. Kumar, “UAVs as remote sensing platform in glaciology: Present applications and future prospects,” *Remote Sens. Environ.*, vol. 186, pp. 581–595, 2016.
- [12] C. J. Li and H. Ling, “High-resolution, downward-looking radar imaging using a small consumer drone,” in *Proc. IEEE Int. Symp. Antennas Propag. (APSURSI)*, Jun. 2016, pp. 2037–2038.
- [13] G. Ludeno, I. Catapano, G. Gennarelli, F. Soldovieri, A. R. Vetrella, A. Renga, and G. Fasano, “A micro-UAV-borne system for radar imaging: A feasibility study,” in *Proc. 9th Int. Workshop Adv. Ground Penetrating Radar (IWAGPR)*, Jun. 2017, pp. 1–4.

- [14] M. Lort, A. Aguasca, C. Lopez-Martinez, and T. M. Marin, "Initial evaluation of SAR capabilities in UAV multicopter platforms," *IEEE J. Sel. Topics Appl. Earth Observ. Remote Sens.*, vol. 11, no. 1, pp. 127–140, Jan. 2018.
- [15] M.-L. Ding, C.-B. Ding, L. Tang, X.-M. Wang, J.-M. Qu, and R. Wu, "A W-band 3-D integrated mini-SAR system with high imaging resolution on UAV platform," *IEEE Access*, vol. 8, pp. 113601–113609, 2020.
- [16] G. Virone, A. M. Lingua, M. Piras, A. Cina, F. Perini, J. Monari, F. Paonessa, O. A. Peverini, G. Addamo, and R. Tascone, "Antenna pattern verification system based on a micro unmanned aerial vehicle (UAV)," *IEEE Antennas Wireless Propag. Lett.*, vol. 13, pp. 169–172, 2014.
- [17] M. Garcia, Y. Alvarez, A. Arboleya, B. Gonzalez, Y. R. Vaqueiro, E. de Cos, and F. Las-Heras, "Antenna diagnostics and characterization using unmanned aerial vehicles," *IEEE Access*, vol. 5, pp. 23562–23575, 2017.
- [18] M. Gharibi, R. Boutaba, and S. L. Waslander, "Internet of drones," *IEEE Access*, vol. 5, pp. 22166–22176, 2017.
- [19] D. Palma, A. Zolich, Y. Jiang, and T. A. Johansen, "Unmanned aerial vehicles as data mules: An experimental assessment," *IEEE Access*, vol. 5, pp. 2169–3536, 2017.
- [20] P. G. de Santos, E. Garcia, J. Estremera, and M. A. Armada, "DYLEMA: Using walking robots for landmine detection and location," *Int. J. Syst. Sci.*, vol. 36, no. 9, pp. 545–558, Jul. 2005.
- [21] A. Ismail, M. Elmogy, and H. ElBakry, "Landmines detection using autonomous robots: A survey," *Int. J. Emerg. Trends Technol. Comput. Sci.*, vol. 3, pp. 183–187, Oct. 2014.
- [22] (Oct. 2017). *Minekafon Project*. [Online]. Available: <http://minekafon.org/>
- [23] A. Amiri, K. Tong, and K. Chetty, "Feasibility study of multi-frequency ground penetrating radar for rotary UAV platforms," in *Proc. IET Int. Conf. Radar Syst.*, 2012, pp. 1–6.
- [24] E. Schreiber, A. Heinzel, M. Peichl, M. Engel, and W. Wiesbeck, "Advanced buried object detection by multichannel, UAV/drone carried synthetic aperture radar," in *Proc. 13th Eur. Conf. Antennas Propag. (EuCAP)*, 2019, pp. 1–5.
- [25] M. Schartel, R. Burr, W. Mayer, N. Docci, and C. Waldschmidt, "UAV-based ground penetrating synthetic aperture radar," in *IEEE MTT-S Int. Microw. Symp. Dig.*, Apr. 2018, pp. 1–4.
- [26] M. Schartel, R. Burr, R. Bähnemann, W. Mayer, and C. Waldschmidt, "An experimental study on airborne landmine detection using a circular synthetic aperture radar," 2020, *arXiv:2005.02600*. [Online]. Available: <http://arxiv.org/abs/2005.02600>
- [27] D. Sipos, P. Planinsic, and D. Gleich, "On drone ground penetrating radar for landmine detection," in *Proc. 1st Int. Conf. Landmine, Detection, Clearance Legislations (LDCL)*, Apr. 2017, pp. 1–4.
- [28] D. Šipoá and D. Gleich, "A lightweight and low-power UAV-borne ground penetrating radar design for landmine detection," *Sensors*, vol. 20, no. 8, p. 2234, Apr. 2020.
- [29] J. Colorado, M. Perez, I. Mondragon, D. Mendez, C. Parra, C. Devia, J. Martinez-Moritz, and L. Neira, "An integrated aerial system for landmine detection: SDR-based ground penetrating radar onboard an autonomous drone," *Adv. Robot.*, vol. 31, no. 15, pp. 791–808, Aug. 2017.
- [30] (Oct. 2017). *Drone Equipped With Ground Penetrating Radar*. [Online]. Available: <https://www.uavvision.com/2017/10/18/drone-equipped-with-ground-penetrating-radar-gpr/>
- [31] M. Garcia-Fernandez, Y. Alvarez-Lopez, A. Arboleya-Arboleya, B. Gonzalez-Valdes, Y. Rodriguez-Vaqueiro, F. Las-Heras, and A. Pino-Garcia, "Synthetic aperture radar imaging system for landmine detection using a ground penetrating radar on board a unmanned aerial vehicle," *IEEE Access*, vol. 6, pp. 45100–45112, 2018.
- [32] M. Garcia-Fernandez, Y. Alvarez-Lopez, and F. Las-Heras, "Autonomous airborne 3D SAR imaging system for subsurface sensing: UWB-GPR on board a UAV for landmine and IED detection," *Remote Sens.*, vol. 11, p. 2357, 2019.
- [33] (May 2020). *UAV Microcontroller From Emlid*. [Online]. Available: <https://emlid.com/navio/>
- [34] (May 2020). *GNSS-RTK From Topcon*. [Online]. Available: <https://www.topconpositioning.com/oem-components-technology/>
- [35] (May 2020). *Explore UWB Radar From ILMSens*. [Online]. Available: <https://www.ilmsens.com/products/m-explore/>
- [36] (May 2020). *TSA 600 Vivaldi Antenna From RF Space*. [Online]. Available: [http://rfospace.com/RFSPACE/Antennas\\_files/TSA600.pdf](http://rfospace.com/RFSPACE/Antennas_files/TSA600.pdf)
- [37] (May 2020). *Spreading Windws s1000+ From DJI*. [Online]. Available: <https://www.dji.com/spreading-wings-s1000-plus>
- [38] M. Garcia-Fernandez, Y. Alvarez-Lopez, and F. L. Heras, "3D-SAR processing of UAV-mounted GPR measurements: Dealing with non-uniform sampling," in *Proc. 14th Eur. Conf. Antennas Propag. (EuCAP)*, Mar. 2020, pp. 1–5.
- [39] (Dec. 2018). *HMA Global Sops 2018. Chapter 6: Search and Clearance from Humanitarian Mine Action*, by Andy Smith. [Online]. Available: [https://nolandmines.com/Global\\_SOPs/V3.0\\_Global\\_SOPs\\_Chap\\_6\\_Search\\_and\\_Clearance.pdf](https://nolandmines.com/Global_SOPs/V3.0_Global_SOPs_Chap_6_Search_and_Clearance.pdf)



**MARÍA GARCÍA-FERNÁNDEZ** was born in Luarca, Spain, in 1992. She received the M.Sc. and Ph.D. degrees in telecommunication engineering from the University of Oviedo, Spain, in 2016 and 2019, respectively. Since 2013, she has been involved in several research projects with the Signal Theory and Communications Research Group, TSC-UNIOVI, University of Oviedo. She was a Visiting Student with Stanford University, Palo Alto, CA, USA, in 2013 and 2014, a Visiting Scholar with the Gordon Center for Subsurface Sensing and Imaging Systems, Northeastern University, Boston, MA, USA, in 2018, and a Visiting Researcher at the Radar Department of TNO, The Hague, The Netherlands, in 2019. Her current research interests include inverse scattering, remote sensing, radar systems, imaging techniques, antenna measurement and diagnostics, and non-invasive measurement systems on board unmanned aerial vehicles. She was a recipient of the 2020 National Award to the Best Ph.D. Thesis on Telecommunication Engineering (category: telecommunications technologies and applications).



**YURI ÁLVAREZ LÓPEZ** (Senior Member, IEEE) received the M.S. and Ph.D. degrees in telecommunication engineering from the University of Oviedo, Spain, in 2006 and 2009, respectively. He was a Visiting Scholar with the Department of Electrical Engineering and Computer Science, Syracuse University, Syracuse, USA, in 2008, a Visiting Postdoc at the Gordon Center for Subsurface Sensing and Imaging Systems (CenSSIS) ALERT Center of Excellence, Northeastern University, Boston, USA, from 2011 to 2014, and a Visiting Postdoc at the ELEDIA Research Center, Trento, Italy, in 2015. He has been with the Signal Theory and Communications research group of the University of Oviedo, Gijón, Spain, since 2006, where he is currently a Professor. His research interests include antenna diagnostics, antenna measurement techniques, RF techniques for indoor location, inverse scattering and imaging techniques, and phaseless methods for antenna diagnostics and imaging. He was a recipient of the 2011 Regional and National Awards to the Best Ph.D. Thesis on Telecommunication Engineering (category: security and defense).



**FERNANDO LAS-HERAS ANDRÉS** (Senior Member, IEEE) received the M.S. and Ph.D. degrees in telecommunication engineering from the Technical University of Madrid (UPM), in 1987 and 1990, respectively. He was a National Graduate Research Fellow, from 1988 to 1990, and an Associate Professor with the Department of Signal, Systems and Radiocommunications of the UPM, from 1991 to 2000. From December 2003, he holds a Full-Professor position at the University of Oviedo, where he was the Vice-dean for Telecommunication Engineering at the Technical School of Engineering, Gijón, from 2004 to 2008. As of 2001, he heads the research group Signal Theory and Communications TSC-UNIOVI at the Department of Electrical Engineering of the University of Oviedo. He was a Visiting Lecturer with the National University of Engineering, Peru, in 1996, a Visiting Researcher with Syracuse University,

New York, in 2000, and a short term Visiting Lecturer with ESIGELEC, France, from 2005 to 2011. He held the Telefónica Chair on RF Technologies, ICTs applied to Environment and ICTs and Smartcities at the University of Oviedo, from 2005 to 2015. A member of the Board of Directors of the IEEE Spain Section, from 2012 to 2017, and a Vice-President, from 2020 to 2022, of the board of the joint IEEE MTT-S (Microwave Theory and Techniques) and AP-S (Antennas and Propagation) Spain Chapter, a member of the Science, Technology and Innovation Council of Asturias, from 2010 to 2012, and a President of the professional association of Telecommunication Engineers at Asturias. He has led and participated in a great number of research projects and has authored over 200 journal articles and over 250 at international conferences on antennas, metamaterials, and inverse problems with application to antenna measurement, electromagnetic imaging and localization, developing computational electromagnetics algorithms and technology on microwaves, millimeter wave, and THz frequency bands.

• • •